PHYSICAL REVIEW A **94**, 053846 (2016)

Noncollinear wave mixing of attosecond XUV and few-cycle optical laser pulses in gas-phase atoms: Toward multidimensional spectroscopy involving XUV excitations

Wei Cao,[1,2,3] Erika R. Warrick,[1,2] Ashley Fidler,[1,2] Daniel M. Neumark,[1,2] and Stephen R. Leone[1,2,3]
[1]*Chemical Sciences Division, Lawrence Berkeley National Laboratory, Berkeley, California 94720, USA*
[2]*Department of Chemistry, University of California, Berkeley, California 94720, USA*
[3]*Department of Physics, University of California, Berkeley, California 94720, USA*
(Received 20 September 2016; published 23 November 2016)

Ultrafast nonlinear spectroscopy, which records transient wave-mixing signals in a medium, is a powerful tool to access microscopic information using light sources in the radio-frequency and optical regimes. The extension of this technique towards the extreme ultraviolet (XUV) or even x-ray regimes holds the promise to uncover rich structural or dynamical information with even higher spatial or temporal resolution. Here, we demonstrate noncollinear wave mixing between weak XUV attosecond pulses and a strong near-infrared (NIR) few-cycle laser pulse in gas phase atoms (one photon of XUV and two photons of NIR). In the noncollinear geometry the attosecond and either one or two NIR pulses interact with argon atoms. Nonlinear XUV signals are generated in a spatially resolved fashion as required by phase matching. Different transition pathways can be identified from these background-free nonlinear signals according to the specific phase-matching conditions. Time-resolved measurements of the spatially gated XUV signals reveal electronic coherences of Rydberg wave packets prepared by a single XUV photon or XUV-NIR two-photon excitation, depending on the applied pulse sequences. These measurements open possible applications of tabletop multidimensional spectroscopy to the study of dynamics associated with valence or core excitation with XUV photons.

DOI: 10.1103/PhysRevA.94.053846

I. INTRODUCTION

Nonlinear multidimensional spectroscopy has advanced dramatically from early work on nuclear magnetic resonance [1] using radio frequencies to many applications in the optical regime [2,3] including photon echoes [4], transient gratings [5], coherent anti-Stokes-Raman scattering [6–8], and multidimensional infrared (IR) spectroscopy [9–12]. The wavelength and the cycle period of the applied electromagnetic fields set limits on the spatial resolution for structural imaging purposes and on the temporal resolution for tracking dynamical evolution. For example, radio frequencies probe electron spin dynamics with a characteristic time of milliseconds, whereas femtosecond dynamics, such as electronic and vibrational motions in molecules, become accessible when optical pulses are used [7,8,13]. Extending ultrafast nonlinear spectroscopy to extreme ultraviolet (XUV) or even shorter wavelengths is of particular importance for probing valence or core excitation dynamics with unprecedented time resolution. In this paper, we demonstrate a tabletop nonlinear spectroscopy scheme in the XUV region for studying electronic ultrafast dynamics.

Although the potential significance of using short-wavelength photons has been proposed in a number of theoretical works [14–17], implementing the XUV analog of conventional optical methods has been challenging due to the lack of intense coherent XUV sources. The first experimental demonstration of a XUV transient grating was realized only recently using a free-electron laser (FEL) source at microjoule pulse energies. That suboptical wavelength transient grating initiated molecular vibrations in a SiO_2 sample with nanometer resolution and opened the possibility for investigating charge-transfer dynamics in solids [18].

Nonlinear XUV spectroscopy can also be carried out with laser-driven high-order harmonic generation (HHG), the basis of a tabletop coherent XUV source that complements the large-scale FEL facilities. HHG can form attosecond light bursts [19,20] and thus offers superb timing probes, compared to FELs, which have typical pulse durations of a few tens of femtoseconds or longer. The drawback of HHG is its low conversion efficiency [21,22], which generally produces pulses too weak to perform XUV-only nonlinear spectroscopy. However, by combining HHG with commercially available strong optical laser pulses, appreciable nonlinear wave-mixing processes involving a HHG photon can be induced in gas media, providing a sensitive XUV probe for electronic dynamics. Time-resolved heterodyne wave-mixing spectroscopy using collinear HHG and near-infrared (NIR) pulses as the driving sources [i.e., attosecond transient absorption spectroscopy (ATAS)] has revealed the laser-coupled electronic dynamics of valence [23–28] and inner-valence electrons [29] in atoms as well as vibrational coherences in molecules [30–32]. The detected XUV light in ATAS is a coherent superposition of the original HHG pulse E_{HHG} (the local oscillator) and the generated dipole radiation E_g. The dipole response in ATAS consists of multiple components, including the linear response corresponding to the absorption of a HHG photon, the near-resonant third-order response corresponding to the effect of one XUV and two NIR photons, and the nonresonant nonlinear response, such as the Stark effect. Interference between the multiple components gives rise to rich features in the XUV spectrum [24,28]. However, this very richness makes it challenging to extract quantitative dynamic information encoded in the complex spectrum.

Recently, a homodyne four-wave-mixing (FWM) measurement in neon using a spectrally shaped XUV attosecond pulse train has been reported [33]. A phase-matched FWM signal in the XUV that is almost background free is generated in a collinear geometry by filtering certain incident frequencies. In contrast with ATAS, the detected XUV light is the background-free FWM signal, which thus contains clean dynamic information on the field-free wave packet

 ©2016 American Physical Society

that is launched by the HHG pulse. This measurement has considerable potential for applications of new XUV frequency generation as well as tracing isolated dynamical pathways. However, the HHG field in the collinear homodyne FWM experiment is spectrally shaped such that the newly generated frequency components do not exist in the original harmonic spectrum. This requirement hinders the general application of this technique using an arbitrary HHG spectrum.

In this paper, we report time-resolved homodyne XUV wave-mixing spectroscopy with an arbitrary high harmonic spectrum using a much more versatile noncollinear geometry. In the wave-mixing gas medium, the NIR pulse is intersected with the HHG pulse at an angle (18 mrad), and nonlinear wave-mixing signals are generated in a spatially resolved fashion due to phase-matching conditions. Different NIR-induced transition pathways, such as Λ- or V-type transitions and ladder-type transitions, are linked to the nonlinear signals that are emitted at different angles, therefore, allowing one to study the dynamics of isolated quantum pathways. We use argon as an example to investigate the separation of different wave-mixing processes and the tracking of electronic coherences of Rydberg wave packets prepared by one HHG photon, i.e., the bright state quantum beat. By introducing a second NIR pulse coinciding with the HHG pulse in time, HHG plus NIR, two-photon-induced electronic coherences, i.e., dark-state quantum beats, can be singled out and studied. Using multiple independent NIR pulses as mixing sources opens new possibilities for applying tabletop multidimensional spectroscopy to the investigation of valence excited or core excited electronic dynamics initiated by XUV light sources.

II. EXPERIMENTAL METHOD

The experimental setup is shown in Fig. 1. The 800-nm 25-fs laser pulse from a Ti:sapphire laser amplifier without carrier envelope phase stabilization (Femtopower) is spectrally broadened (spanning from 550 to 950 nm) by a neon-filled hollow core fiber. A set of chirped mirrors (Ultrafast Innovations) compresses the NIR pulse down to 6 fs, which is characterized using an autocorrelator (Femtometer). The majority of the few-cycle NIR pulse energy (300 μJ) is focused into a xenon gas cell for high-order harmonics generation. The generated harmonics pass through a retractable metal filter to block the residual NIR driving field; experiments can be carried out with this filter in place or removed (see below). A replica of the few-cycle NIR pulse is picked off from the original pulse and combined with the HHG attosecond pulses with a hole mirror. The NIR pulse is displaced from the center of the hole mirror while the HHG passes through the hole. As a result both the HHG and the NIR pulses propagate noncollinearly and intersect at the interaction region with a crossing angle of 18 mrad, which is deduced from the interference pattern between the NIR pulse used for harmonic generation and the delayed NIR pulse used for wave mixing. The intensity of the NIR pulse inside the argon gas cell is approximately 2×10^{12} W/cm^2. The gas pressure is 8 Torr. After the wave-mixing gas cell the spectrum in the XUV region is recorded by an XUV spectrometer consisting of a flat field grating and a CCD camera. The resolution of the spectrometer is 14 meV at 14 eV.

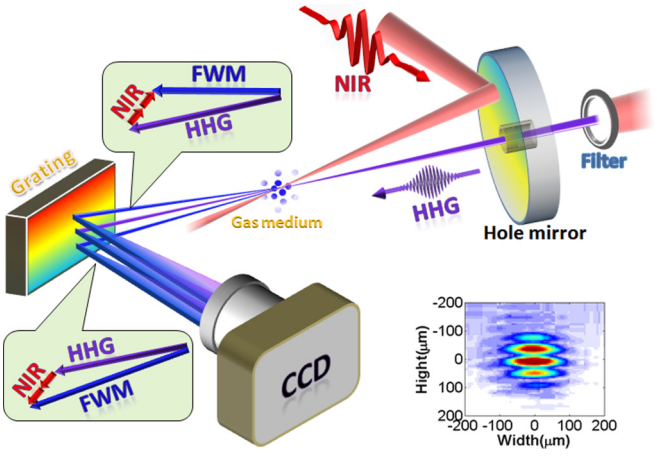

FIG. 1. Schematic of the noncollinear transient wave-mixing spectroscopy. The NIR pulse intersects with the HHG pulse at an angle, and the phase-matching condition determines the direction of the emitted FWM signals. The bottom right panel shows the interference pattern of the two NIR pulses when the metallic filter is removed. The vertical camera pixel size is 5.2 μm.

III. EXPERIMENTAL RESULTS

A. Spatially resolved wave mixing with one NIR pulse

In the first type of experiment, we demonstrate noncollinear XUV spectroscopy in argon using one NIR laser beam and one HHG beam. Each CCD camera image is recorded with 5000 laser pulses throughout the paper. The XUV [see Fig. 2(a)] contains multiple harmonic orders and has a divergence of roughly 2 mrad. When the NIR pulse arrives during or after the HHG pulse, the HHG-NIR wave-mixing process is switched on. As shown in Fig. 2(b), the transmitted XUV spectrum shows strong modulation along the on-axis direction because of the interference between the HHG pulse and the generated dipole radiation. In addition, off-axis narrow-divergence signals appear at energies corresponding to atomic transitions in argon. Depending on the photon energy, the off-axis signals appear above (around 12 eV) or below (about 15 eV) the HHG beam. The signals at different emission angles in Fig. 2(b) correspond to different nonlinear dipole responses as discussed below.

By applying spatial filters to the image in Fig. 2(b), the time evolution of specific emission features can be examined. Figure 3 shows the delay-dependent absorption spectrum of the on-axis signals. For high-lying Rydberg states (between 14.5 and 15.75 eV), the spectrogram shows non-Lorentzian line shapes as well as hyperbolic sidebands built upon resonant states for early delays (<80 fs).

Figure 4 shows the delay-dependent intensities of the spatially gated off-axis signals (integrated over 1 mrad) as well as their Fourier analysis. The upper branch off-axis signals (with energies near the $4d/5d$ Rydberg series) show very regular modulation periods [Fig. 4(a)], and the Fourier analysis shows that they share a common oscillation frequency of 0.21 eV (20 fs). The delay-dependent intensities of the lower branch off-axis signals [Fig. 4(c)] show a more compli-

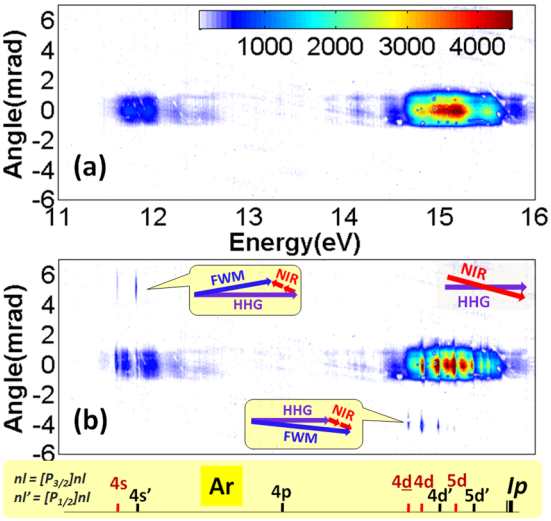

FIG. 2. (a) A two-dimensional (2D) image of the XUV-only spectrum. The inset shows the propagation directions of HHG and NIR pulses in this experiment. (b) A 2D image of the transmitted XUV spectrum after the nonlinear wave mixing in the argon gas. The NIR pulse overlaps with the HHG pulse in time. Phase-matching diagrams of the newly generated XUV light via the FWM are shown in the yellow boxes. The corresponding dipole-allowed transitions of argon $3s^2 3p^6$ to $3s^2 3p^5[^2P_{3/2,1/2}]nl$ are shown at the bottom. The $nd[1/2]$ and $nd[3/2]$ states that converge to the same $^2P_{3/2}$ limit are labeled $n\underline{d}$ and nd, respectively.

cated structure comprising multiple oscillation frequencies [Fig. 4(d)].

B. Spatially resolved wave mixing with two NIR pulses

In the second type of experiment, we demonstrate noncollinear wave mixing using two separate NIR laser pulses together with the HHG pulse. To implement this, we remove the metallic filter in Fig. 1 to unblock the NIR driving field that is used for high-order harmonic generation. This introduces an additional NIR pulse into the wave-mixing

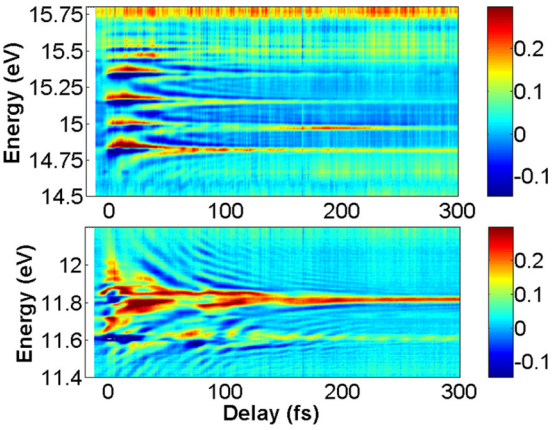

FIG. 3. The delay-dependent absorption spectrum (integrated from −1 to +1 mrad) of argon in terms of optical density: $-\log_{10}(\frac{I_t}{I_0})$, where I_0 and I_t are the spectral densities before and after the gas cell, respectively.

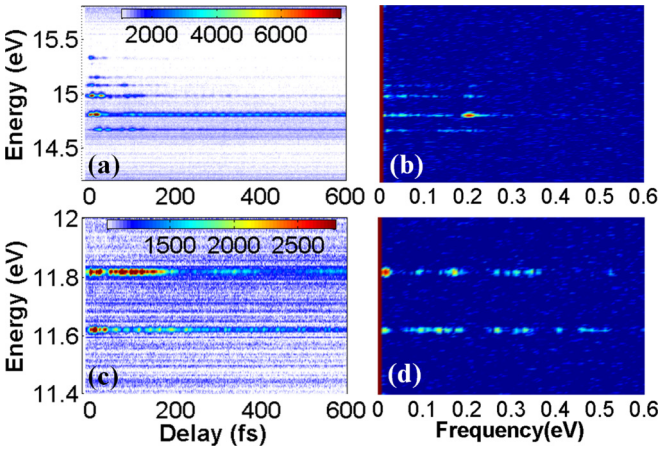

FIG. 4. (a) An XUV spectrum of the lower branch off-axis signals in Fig. 2(b) as a function of HHG-NIR delay. (b) Fourier analysis (logarithm) of the spectrogram in (a) with respect to the delay axis. (c) An XUV spectrum of the upper branch off-axis signals in Fig. 2(b) as a function of HHG-NIR delay. (d) Fourier analysis (logarithm) of the spectrogram in (c) with respect to the delay axis. Positive delays mean the HHG attosecond pulse precedes the NIR pulse

gas cell that is spatiotemporally overlapped and propagates collinearly with the HHG pulse. Hereafter, the NIR pulse that crosses with the HHG beam at an angle and the NIR pulse collinear with the HHG beam are labeled as IR_{Ang} and IR_{Col}, respectively. The intensity of IR_{Col} is approximately 2×10^{11} W/cm^2 at the wave-mixing gas cell.

Two-dimensional images of the transmitted XUV spectrum using two NIR pulses are shown in Fig. 5. When the two few-cycle NIR pulses overlap in time, the transmitted XUV light shows a diffraction pattern near the atomic Rydberg state transitions as seen in Fig. 5(a). It consists of multiple sidebands

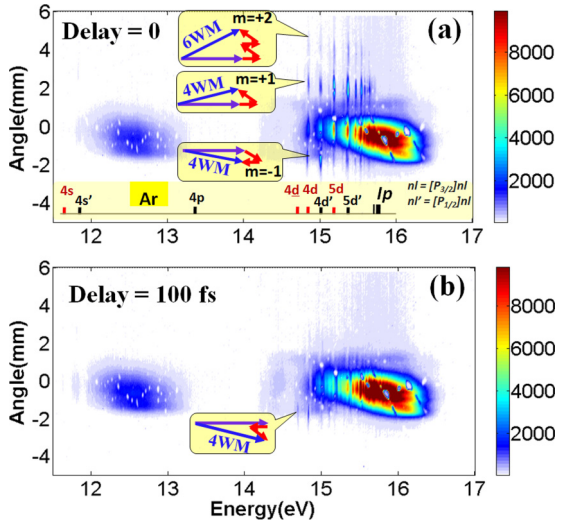

FIG. 5. The 2D images of the transmitted XUV spectrum after nonlinear wave mixing in argon gas when two NIR pulses are present. The angled NIR pulse arrives at (a) and after (b) the HHG pulse. The yellow boxes indicate the phase-matching diagrams of the newly generated off-axis XUV signals. The purple arrows stand for the HHG wave vectors, and the red arrows stand for the NIR wave vectors.

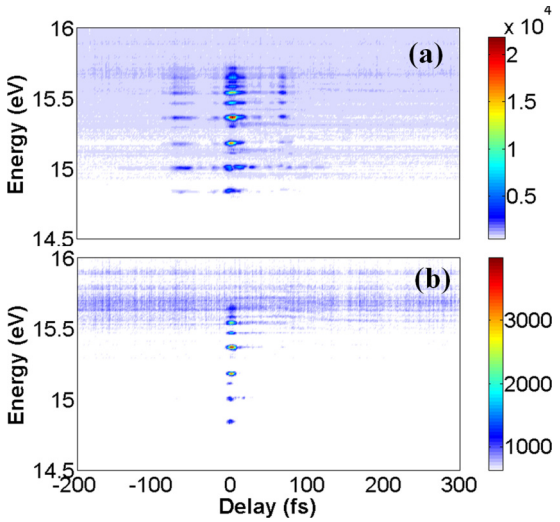

FIG. 6. Delay-dependent intensity of off-axis FWM signals (a) for $m = +1$ and six-wave-mixing signals (b) for $m = +2$.

above the HHG beam and predominantly a single one below. Such a diffraction pattern disappears at larger delays, and only the relatively weaker off-axis signals near the $4d$ transitions below the HHG beam persist [Fig. 5(b)].

The time-resolved XUV signals from different diffracted sidebands [labeled $m = +1, +2, -1$ in Fig. 5(a)] are shown in Figs. 6 and 7. The diffracted XUV signal for sidebands $m = +1$ and $m = +2$ are seen only when the NIR pulses overlap (Fig. 6). This indicates that both $\mathrm{IR_{Ang}}$ and $\mathrm{IR_{Col}}$ have to coincide in time in order to trigger the nonlinear process. In contrast, the diffracted XUV signals for sideband $m = -1$ persist when $\mathrm{IR_{Ang}}$ arrives after the $\mathrm{HHG/IR_{Col}}$ pulses for energies below 15.4 eV. In addition, the delay-dependent

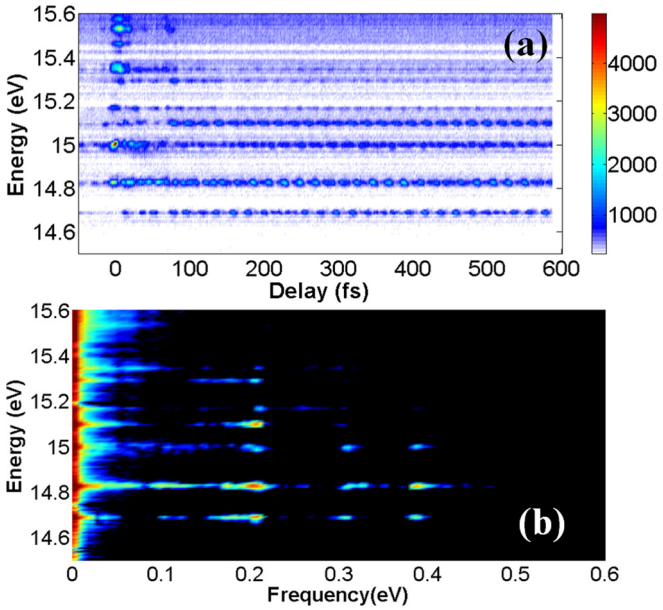

FIG. 7. (a) Delay-dependent intensity of off-axis FWM signals for $m = -1$ in Fig. 5. (b) Fourier analysis (logarithm) of the spectrogram in (a) with respect to the delay axis.

signals for sideband $m = -1$ show periodic modulations. The Fourier analysis of these modulations [Fig. 7(b)] reveals mainly three common frequencies: 0.21, 0.31, and 0.39 eV.

IV. DISCUSSION

The time-dependent on-axis signals shown in Fig. 3 are mainly from the ac Stark effect. The HHG pulse first populates the Rydberg states and initiates radiating dipoles; the delayed NIR pulse then imposes a phase promptly on the dipoles due to the nonresonant ac Stark effect. The dipoles induced by this effect propagate collinearly and interfere with the original HHG pulse that is largely unaffected as it passes through the gas medium, giving rise to typical absorption features related to Stark effects, such as line broadening, splitting, shifting, as well as hyperbolic sidebands in the absorption spectrogram [24,34,35]. For the $4s/4s'$ states (11.6 and 11.8 eV), the splitting and shifting in the absorption lines, however, persist for much longer delays (>150 fs), and this is due to resonant processes, such as Rabi cycling dominating over the nonresonant ac Stark effect for the low-lying excited states, and therefore the corresponding line shapes are more sensitive to the electric field than to the intensity profile of the NIR pulse. Such delay-dependent structures of the on-axis signals are similar to the previously reported results of argon using attosecond transient absorption spectroscopy [28]. However, multiple effects, such as the ladder- or V-type population transfer and ac Stark effects can contribute simultaneously in the ATAS experiment, whereas under the noncollinear wave-mixing arrangement the ac Stark effect is the dominant signature for the on-axis signal.

The more interesting off-axis emission features observed here can be understood based on energy conservation and phase matching (momentum conservation). In the case when only one NIR pulse is present, the off-axis signals below the HHG beam [negative angle in Fig. 2(b)] arise from the polarization dipole formed by the coherence between the excited states around 15 eV [$4d/4d'$, $5d/5d'$, and $6s/6s'$ (not labeled) manifolds] and the ground state of argon atoms. This coherence can be induced by a FWM process in which the HHG pulse populates both the $4s$ and the $4s'$ states coherently in argon, then the NIR pulse transfers part of the populations of both states into the same final state around 15 eV via a two-photon transition. This population transfer process is enhanced due to the presence of a $4p$ dark state that is coupled resonantly with the $4s$ and $4d/5d$ manifolds by the NIR pulse. The direction of these nonlinear signals is determined by the phase-matching diagram as shown in Fig. 2(b). With a crossing angle of $\alpha = 18$ mrad between the NIR and the HHG pulses, the FWM signal corresponding to the $2p - 4s'$ transition (11.8 eV) is emitted at an angle of about $\theta \approx \alpha \frac{11.8-15}{15} = -3.84$ mrad. The experimentally observed emission angles agree well with the values predicted by the phase-matching diagrams, providing convincing evidence that the off-axis signals are dominated by the FWM processes. The phase difference of the two three-photon processes (via $4s$ and $4s'$) has a linear relationship with the HHG-NIR delay, leading to constructive and destructive interferences alternately as the delay increases. Therefore, the intensities of the nonlinear signals corresponding to different final states ($4d/5d$ Rydberg

series) in Fig. 4(a) share a common oscillation frequency of 0.21 eV (20-fs period) as shown in Fig. 4(b). This value is the energy separation of the two spin-orbit split states $4s$ and $4s'$, representing the quantum beat of the simplest wave packet formed by the coherent superposition of two states prepared by the HHG photon. This observation is similar to that reported in the collinear homodyne FWM spectroscopy in neon [33].

Following the same arguments, the off-axis signals above the HHG beam [positive angle in Fig. 2(b)] at 11.8 eV, the $2p-4s'$ transition, reflects a pathway of resonantly absorbing a HHG photon (around 15 eV) and emitting two NIR photons. The emission direction of the nonlinear XUV signal is expected to be around $\theta \approx \alpha \frac{15-11.8}{11.8} = 4.88$ mrad, agreeing well with the observed value. The delay-dependent intensities of these nonlinear signals at the $2p-4s/4s'$ transition energies show a complicated structure consisting of multiple oscillating frequencies [see Fig. 4(d)]. Similar to the case of Fig. 4(a), these frequencies represent the quantum beats of a more complicated wave packet initiated by the HHG pulse, formed by the coherent superposition of multiple congested Rydberg states around 15 eV that include the $4d/4d'$, $5d/5d'$, and $6s/6s'$ manifolds. Note that in both Figs. 4(a) and 4(c) the signals at early delays are relatively stronger than those at long delays. This enhancement is likely due to the contribution from processes where the HHG photon is absorbed nonresonantly in the presence of the NIR pulse. The few-cycle NIR pulse can have satellite pulses and long pedestals because of noncompensated higher-order dispersion, and such nonresonant enhancement of the FWM signal can last for rather long delays.

Phase matching requires that the angle between the FWM signal and the HHG beam is proportional to the energy difference of the two states coupled by the two NIR photons. In the above-mentioned FWM processes, the NIR pulse couples the two excited states separated by about 3.2 eV via a ladder-type transition, giving rise to the off-axis wave-mixing signals that are well separated from the HHG beam. For FWM processes in which the NIR pulse couples two degenerate or near-degenerate energy levels, the emission angle of the FWM signal is expected to be close to that of the HHG beam. Therefore, nonlinear signals responsible for V- or Λ-type population transfer processes should also contribute to the on-axis signals in Fig. 2(b). However, these signals are overshadowed by the strong background associated with the nonresonant Stark effect, often preventing the decisive identification of such V- or Λ-type population transfer pathways. A careful Fourier analysis is required to pinpoint such physical processes as demonstrated in Ref. [28].

In conventional attosecond transient absorption spectroscopy, the dipole responses of the medium to the external electromagnetic field give rise to signals propagating collinearly with the HHG and NIR pulses and therefore are indistinguishable. The analysis of Figs. 2 and 4 demonstrates that, under the noncollinear geometry, the mixed nonlinear dipole responses can be separated spatially, thus, allowing one to study dynamics associated with isolated quantum pathways.

The experiments in Sec. III A demonstrate noncollinear XUV spectroscopy using one HHG pulse and two photons from one NIR pulse as the driving sources. Spatially resolved background-free FWM signals are generated, allowing one to single out the individual quantum pathway and study the related dynamics. In such a configuration, the NIR pulse is acting as a probe that interacts with the medium twice within the pulse duration, and the probed dynamics is the quantum beat of the bound-state wave packet prepared by absorption of a single XUV photon.

In the experiments in Sec. III B where two different NIR pulses are used (Fig. 5), the two NIR pulses interfere and form an intensity modulation at the overlap region along the direction $\vec{k}_g = \vec{k}_{\mathrm{IR1}} - \vec{k}_{\mathrm{IR2}}$, where $\vec{k}_{\mathrm{IR1}}, \vec{k}_{\mathrm{IR2}}$ stand for the wave vectors of the two NIR pulses. After the HHG pulse populates the Rydberg states and induces the polarization dipole, one of the major effects of the NIR pulses is to promptly impose a phase that is approximately proportional to the NIR intensity on the dipole [34,35], effectively changing the optical property of the medium for electromagnetic fields with frequencies equal to the atomic transitions. This means that the intensity modulation created by the two coinciding NIR pulses is acting as a transient grating for the incident HHG photon and the diffracted angle of the XUV light can be predicted by the grating equation: $\vec{k}_{\mathrm{diff}} = \vec{k}_{\mathrm{HHG}} - m\vec{k}_g$. Here $\vec{k}_{\mathrm{diff}}, \vec{k}_{\mathrm{HHG}}$ indicate the wave vectors of the diffracted and incident XUV photons, respectively, and m is an integer specifying the diffraction order. With a central wavelength of 750 nm for the NIR pulses, the diffracted angle of the 15-eV XUV photon is estimated to be $\sim$2.0 mrad for $m = \pm 1$ and $\sim$4 mrad for $m = +2$, in good agreement with the observed angles in Fig. 5(a). Note that the grating equation is equivalent to the phase-matching diagrams of the four-wave-mixing ($m = \pm 1$) and six-wave-mixing ($m = +2$) processes as shown in Fig. 5(a); the two NIR photons for each phase-matching diagram are interchangeable for zero delay. This observation shows the nontrivial contribution of higher-order wave-mixing processes. It also illustrates one of the applications of noncollinear XUV spectroscopy with two NIR pulses: spatially disentangling the dipole responses involving different numbers of photons.

The XUV signals gated on diffraction order $m = +1$ [Fig. 6(a)] and $m = +2$ [Fig. 6(b)] exist only at near-zero time delays where the individual NIR pulses can interact with the medium multiple times cooperatively to induce the desired phase-matching processes. As the delay goes beyond the overlap region, the $m = +2$ (six-wave-mixing) and higher-order channels are terminated because the phase-matching diagrams cannot be satisfied when $\mathrm{IR_{Col}}$ precedes $\mathrm{IR_{Ang}}$. For the lowest-order nonvanishing nonlinear process FWM, additional resonant intermediate states populated by the $\mathrm{HHG/IR_{Ang}}$ pulse pair are required to generate persistent off-axis signals. Figure 6 shows that no resonant dark states exist to assist the $m = +1$ and $m = +2$ diffracted signals beyond zero delay. These measurements essentially provide the convolution of the two NIR pulses. In the four-wave-mixing channel [Fig. 6(a)], satellite pulses that are roughly 75 fs apart from the main pulse are correspondingly observed. In the six-wave-mixing channel [Fig. 6(b)], signatures of satellite pulses are strongly suppressed due to the higher-order nonlinear processes.

The observed persistent diffracted signals at diffraction order $m = -1$ indicate that the $\mathrm{HHG/IR_{Col}}$ pulse pair prepares

multiple long-lived intermediate states that can be interrogated by the delayed probe IR_{Ang}. According to the energy levels of argon as shown in Fig. 5(a), the viable intermediate states are the $4p$ manifold lying around 13.3 eV. They can be accessed by absorbing a 15-eV photon from the HHG pulse and emitting one NIR photon stimulated by IR_{Col}. The long-lived $4p$ states can be excited to the $4d$ states by the probe pulse IR_{Ang} resonantly to complete the FWM process. The related phase-matching diagram for such a FWM pathway indicates that it can only be responsible for diffraction order $m = -1$. This explains the observed diffraction pattern of the XUV light in Fig. 5(b). The arrangement of the pulse sequence determines which diffraction order can persist as the delay increases. If IR_{Col} were to be delayed with respect to the HHG/IR_{Ang} pulse pair instead, we would expect to see persistent XUV signals for diffraction order $m = +1$.

XUV signals at diffraction order $m = -1$ show persistent oscillations for energies below 15.4 eV (Fig. 7). As discussed above, these signals result from the resonant FWM process mediated by the $4p$ dark states, which are initiated by the HHG/IR_{Col} pulse pair. The energy range of the $4p$ states is from 12.9 to 13.48 eV; the IR_{Ang} pulse (centered around 750 nm) predominantly couples these dark states with bright states lying below 15.2 eV. Signals above 15.4 eV are mainly attributed to nonresonant FWM near the overlap region and show cross-correlation between the two NIR pulses, similar to Fig. 7. The persistent oscillations contain dynamic information of a wave packet that is a coherent superposition of multiple dark states prepared by the HHG and IR_{Col} pulses. The Fourier analysis [see Fig. 7(b)] of these oscillations shows that there are mainly three common frequencies contributing to these oscillations: 0.21, 0.31, and 0.39 eV, which are the beating frequencies of the wave packet. The candidate states to form the dark-state wave packet are as follows: $(^2P_{3/2})4p$ at 13.27 eV, $(^2P_{3/2})4p$ at 13.095 eV, $(^2P_{3/2})4p)$ at 13.17 eV, and $(^2P_{1/2})4p)$ at 13.48 eV. This measurement demonstrates the second application of the noncollinear XUV spectroscopy with two NIR pulses: detecting two-photon-induced electronic coherences.

V. CONCLUSION

We experimentally demonstrate noncollinear time-resolved XUV spectroscopy using HHG attosecond pulses and one or two few-cycle NIR pulses as wave-mixing sources. Using argon atoms as the nonlinear medium, spatially resolved XUV signals that are well separated from the original HHG beam are generated when the HHG and NIR pulses are overlapping in time. The emission angles of the diffracted XUV signals agree well with the values predicted by the phase-matching diagrams, providing evidence that the perturbative four- (six-) wave-mixing processes are responsible for generation of the diffracted light.

Such experiments spatially separate dipole responses that result from different transition pathways, providing background-free nonlinear signals to pinpoint the individual quantum pathways. By delaying the NIR pulse(s) with respect to the HHG pulse, the corresponding dynamics of bound states lying in the XUV region can be probed. When one HHG and one NIR pulse are applied, the detected dynamics represent the quantum beat of the wave packet formed by a coherent superposition of excited states populated by the HHG pulse, a one-photon-induced electronic coherence. When one HHG and two NIR pulses are applied with one NIR pulse synchronized with the HHG pulse, the detected dynamics reflect the quantum beat of a dark-state wave packet that is prepared by the HHG pulse and the synchronized NIR pulse, a two-photon-induced electronic coherence. Although the most prominent information observed from the current experimental method is the electronic quantum beat, extra information, such as the dephasing time of electronic coherence and the lifetime of highly excited states initiated by the XUV photon, is expected to be accessible as well and will be subject to future investigation. Future studies will also include implementing multiple delay-independent few-cycle NIR pulses. By changing the time intervals between pulses independently we expect to access more complicated dynamics with multiple degrees of freedoms in systems, such as molecules. These measurements demonstrate a promising means for tabletop multidimensional spectroscopy involving XUV excitation.

ACKNOWLEDGMENTS

This work was supported by the Director, Office of Science, Office of Basic Energy Sciences and by the Division of Chemical Sciences, Geosciences, and Biosciences of the U.S. Department of Energy at LBNL under Contract No. DE-AC02-05CH11231.

[1] W. P. Aue, E. Bartholdi, and R. R. Ernst, J. Chem. Phys. **64**, 2229 (1976).
[2] N. Bloembergen, Rev. Mod. Phys. **54**, 685 (1982).
[3] S. Mukamel, *Principles of Nonlinear Optical Spectroscopy* (Oxford University Press, Oxford, 1999).
[4] N. A. Kurnit, I. D. Abella, and S. R. Hartmann, Phys. Rev. Lett. **13**, 567 (1964).
[5] E J Brown, Q. Zhang, and M. Dantus, J. Chem. Phys. **110**, 5772 (1999).
[6] W. M. Tolles, J. W. Nibler, J. R. McDonald, and A. B. Harvey, Appl. Spectrosc. **31**, 253 (1977).
[7] C. C. Hayden and D. W. Chandler, J. Chem. Phys. **103**, 10465 (1995).
[8] M. Schmitt, G. Knopp, A. Materny, and W. Kiefer, Chem. Phys. Lett. **270**, 9 (1997).
[9] P. Hamm, M. Lim, and R. M. Hochstrasser, J. Phys. Chem. B **102**, 6123 (1998).
[10] S. Mukamel, Annu. Rev. Phys. Chem. **51**, 691 (2000).
[11] P. Hamm and M. Zanni, *Concepts and Methods of 2D Infrared Spectroscopy* (Cambridge University Press, Cambridge, UK, 2011).
[12] J. C. Wright, Annu. Rev. Phys. Chem. **62**, 209 (2012).

[13] M. Schmitt, G. Knopp, A. Materny, and W. Kiefer, Chem. Phys. Lett. **280**, 339 (1997).
[14] S. Tanaka, V. Chernyak, and S. Mukamel, Phys. Rev. A **63**, 063405 (2001).
[15] S. Tanaka and S. Mukamel, Phys. Rev. Lett. **89**, 043001 (2002).
[16] I. V. Schweigert and S. Mukamel, Phys. Rev. Lett. **99**, 163001 (2007).
[17] S. Mukamel *et al.*, Annu. Rev. Phys. Chem. **64**, 101 (2013).
[18] F. Bencivenga *et al.*, Nature (London) **520**, 205 (2015).
[19] P. Antoine, A. L'Huillier, and M. Lewenstein, Phys. Rev. Lett. **77**, 1234 (1996).
[20] P. M. Paul, E. S. Toma, P. Breger, G. Mullot, F. Augé, P. Balcou, H. G. Muller, and P. Agostini, Science **292**, 1689 (2001).
[21] K. Schiessl, K. L. Ishikawa, E. Persson, and J. Burgdörfer, Phys. Rev. Lett. **99**, 253903 (2007).
[22] E. Constant, D. Garzella, P. Breger, E. Mével, C. Dorrer, C. Le Blanc, F. Salin, and P. Agostini, Phys. Rev. Lett. **82**, 1668 (1999).
[23] A. R. Beck, D. M. Neumark, and S. R. Leone, Chem. Phys. Lett. **624**, 119 (2015).
[24] M. Chini, X. Wang, Y. Cheng, Y. Wu, D. Zhao, D. A. Telnov, S.-I. Chu, and Z. Chang, Sci. Rep. **3**, 1105 (2013).
[25] S. Chen, M. Wu, M. B. Gaarde, and K. J. Schafer, Phys. Rev. A **87**, 033408 (2013).
[26] A. Blättermann, C. Ott, A. Kaldun, T. Ding, and T. Pfeifer, J. Phys. B: At., Mol. Opt. Phys. **47**, 124008 (2014).
[27] A. R. Beck, B. Bernhardt, E. R. Warrick, M. Wu, S. Chen, M. B. Gaarde, K. J. Schafer, D. M. Neumark, and S. R. Leone, New J. Phys. **16**, 113016 (2014).
[28] W. Cao, E. R. Warrick, D. M. Neumark, and S. R. Leone, New J. Phys. **18**, 013041 (2016).
[29] T. Ding *et al.*, Opt. Lett. **41**, 709 (2016).
[30] J. E. Bækhøj, L. Yue, and L. B. Madsen, Phys. Rev. A **91**, 043408 (2015).
[31] M. Reduzzi *et al.*, J. Phys. B: At., Mol. Opt. Phys. **49**, 065102 (2016).
[32] E. R. Warrick, W. Cao, D. M. Neumark, and S. R. Leone, J. Phys. Chem. A **120**, 3165 (2016).
[33] W. Cao, E. R. Warrick, A. Fidler, S. R. Leone, and D. M. Neumark, Phys. Rev. A **94**, 021802(R) (2016).
[34] S. Chen, M. Wu, M. B. Gaarde, and K. J. Schafer, Phys. Rev. A **88**, 033409 (2013).
[35] C. Ott, A. Kaldun, P. Raith, K. Meyer, M. Laux, J. Evers, C. H. Keitel, C. H. Greene, and T. Pfeifer, Science **340**, 716 (2013).